

GALAXY-GALAXY WEAK LENSING MEASUREMENTS FROM SDSS: I. IMAGE PROCESSING AND BASIC RESULTS

WENTAO LUO^{1,4,14}, XIAOHU YANG^{2,3,1}, JUN ZHANG², DYLAN TWEED², LIPING FU⁵, H.J. MO⁶, FRANK C. VAN DEN BOSCH⁷,
CHENGANG SHU⁵, RAN LI⁸, NAN LI^{9,10,11}, XIANGKUN LIU¹², CHUZHONG PAN¹², YIRAN WANG¹³, MARIO RADOVICH^{15,16}

Draft version February 1, 2016

ABSTRACT

As the first paper in a series on studying the galaxy-galaxy lensing from Sloan Digital Sky Survey Data Release 7 (SDSS DR7), we present our image processing pipeline which mainly focuses on correcting the systematics introduced by Point Spread Function (PSF). Using this pipeline, we processed SDSS DR7 imaging data in r band and generated a background galaxy catalog containing the shape information of each galaxy. To assess the quality of our image processing pipeline, we measured the galaxy-galaxy lensing signals around spectroscopic galaxy samples binned in luminosity and stellar mass. Our results are in good agreement with Mandelbaum et al. (2005, 2006) with significantly reduced error bars. The consistency between the two confirms the reliability of our image processing pipeline and initiates our subsequent galaxy-galaxy weak lensing studies.

Subject headings: (cosmology:) gravitational lensing; galaxies: clusters: general

1. INTRODUCTION

Einstein's General Relativity predicted the gravitational lensing effect that light rays from distant sources were bent by foreground massive objects such as galaxies or clusters of galaxies. Yet til 1979 (Walsh et al. 1979) has this theoretical prediction been observationally confirmed. Since then more and more lensing effects were reported either strong e.g., Oguri et al. (2002); Kneib et al. (2004), or weak, e.g. Sheldon et al. (2004); Mandelbaum et al. (2005, 2006); Fu et al. (2008); Bernstein (2009); Cacciato et al. (2009);

Oguri et al. (2009); George et al. (2012); Li et al. (2013); Mandelbaum et al. (2013); Li et al. (2014) from observations such as SDSS, CFHTLS, and SUBARU weak lensing surveys, etc.

As a branch of gravitational lensing, first order weak lensing studies can be further sub-divided to single cluster lensing and galaxy-galaxy lensing. For a deep survey such as CFHTLenS (Heymans et al. 2012), DES (Jarvis et al. 2015), DLS (Wittman et al. 2006), EUCLID (Refregier et al. 2010), LSST (LSST Science Collaboration et al. 2009), KIDS (Kuijken et al. 2015) and SUBARU weak lensing survey (Kaifu 1998; Umetsu 2007), the number density of background galaxy around a single cluster is sufficient to measure the weak lensing signals with high S/N ratio. And further the κ field of the cluster, the mass and the shape of the dark matter contents can be derived (Oguri et al. 2010). Using SUBARU imaging data, Okabe et al. (2014) studied the lensing signals around Coma cluster and selected 32 substructures based on the κ map. For shallower surveys such as SDSS (York et al. 2000), stacked galaxy-galaxy lensing is the only way to measure the weak lensing signals with significant signal to noise ratio. It can also be considered as a powerful tool to measure the mass of dark matter halos around galaxies with certain properties such as luminosity, stellar mass etc. In general, the stacked mass profile around certain lens galaxies is assumed to be isotropic and usually modeled with an NFW (Navarro et al. 1997) profile.

Note that, theoretically, the weak lensing can provide the cleanest measurement of the total mass distribution of the lens system. Whereas halo mass estimation from X ray profile requires the equilibrium assumption of the hot gas (Wang et al. 2014). Satellite kinematics (van den Bosch et al. 2004) and galaxy infall kinematics (Zu & Weinberg 2013; Zu et al. 2014, GIK) information extracted from redshift-space cluster-galaxy cross-correlation function, both of them, assume a virialized scenario of dark matter halos with an isotropic

¹ Key Laboratory for Research in Galaxies and Cosmology, Shanghai Astronomical Observatory, Nandan Road 80, Shanghai 200030, China; E-mail: walt@shao.ac.cn

² Center for Astronomy and Astrophysics, Shanghai Jiao Tong University, Shanghai 200240, China; E-mail: xyang@sjtu.edu.cn

³ IFSA Collaborative Innovation Center, Shanghai Jiao Tong University, Shanghai 200240, China

⁴ Department of Physics, Carnegie Mellon University, Pittsburgh, PA 15213, USA

⁵ Shanghai Key Lab for Astrophysics, Shanghai Normal University, 100 Guilin Road, 200234, Shanghai, China

⁶ Department of Astronomy, University of Massachusetts, Amherst MA 01003-9305, USA

⁷ Department of Astronomy, Yale University, PO Box 208101, New Haven, CT 06520-8101, USA

⁸ Key laboratory for Computational Astrophysics, Partner Group of the Max Planck Institute for Astrophysics, National Astronomical Observatories, Chinese Academy of Sciences, Beijing, 100012, China

⁹ Department of Astronomy & Astrophysics, The University of Chicago, 5640 South Ellis Avenue, Chicago, IL 60637, USA

¹⁰ Argonne National Laboratory, 9700 South Cass Avenue B109, Lemont, IL 60439, USA

¹¹ Kavli Institute for Cosmological Physics at the University of Chicago, Chicago, IL 60637, USA

¹² Department of Astronomy, Peking University, Beijing 100871, China

¹³ Department of Astronomy, University of Illinois at Urbana-Champaign, 1002 W Green St., Urbana, IL 61801, USA

¹⁴ School of Physics, University of Chinese Academy of Sciences, Yuquan Road 19A, Beijing 100049, P.R.China

¹⁵ INFN-Osservatorio Astronomico di Napoli, via Moiraniello 16, I-80131 Napoli, Italy

¹⁶ INFN-Osservatorio Astronomico di Padova, vicolo dell'Osservatorio 5, I-35122 Padova, Italy

Gaussian velocity distribution.

Despite of the promising aspects of weak lensing studies, the actual measurement of the lensing signals demands high accuracy of shape estimation. Along with other systematics such as photometric redshift uncertainties, intrinsic alignment, source selection bias as well as mask effects on peak statistics, etc. (Yang et al. 2003; Mandelbaum et al. 2005, 2006; Yang et al. 2006a; Mandelbaum et al. 2008, 2009a,b; Li et al. 2009; Sheldon et al. 2009; Liu et al. 2014), accurate image measurement always comes to the first in the galaxy-galaxy lensing studies. A weak lensing image processing pipeline, before its application to observational data, should proceed a series of accuracy tests by simulations, e.g. STEP (Shear TESting Program, Heymans et al. 2006; Massey et al. 2007a), Great08 (Bridle et al. 2009), Great 10 (Kitching et al. 2010), GREAT3 (Mandelbaum et al. 2014), Kaggle-the dark matter mapping competition (Supported by NASA & Royal Astronomical Society), as well as other independent software designed for certain surveys, e.g., SHERA (Mandelbaum et al. 2012, hereafter M12).

Many groups have developed image processing pipelines devoting to improve the accuracy of shape measurement for weak lensing studies (Kaiser et al. 1995; Bertin & Arnouts 1996; Maoli et al. 2000; Rhodes et al. 2000; van Waerbeke 2001; Bernstein & Jarvis 2002; Bridle et al. 2002; Refregier 2003; Bacon & Taylor 2003; Hirata & Seljak 2003; Heymans et al. 2005; Zhang 2010, 2011; Bernstein & Armstrong 2014; Zhang et al. 2015). A series of studies on using image moments in Fourier Domain (Zhang 2010, 2011; Zhang et al. 2015) skipped the ellipticity part and directly measured the reduced shear. Lensfit (Miller et al. 2007, 2013; Kitching et al. 2008) applies a Bayesian based model-fitting approach. BFD (Bayesian Fourier Domain) methods (Bernstein & Armstrong 2014) carries out Bayesian analysis in Fourier domain which requires the distribution of unlensed galaxy moments as a prior.

In this paper we focus on establishing an image processing pipeline for weak lensing studies by combining Bernstein & Jarvis (2002, hereafter BJ02) and re-Gaussianization introduced in Hirata & Seljak (2003, hereafter HS03) methods together (hereafter labelled as BJ02+HS03). In section 2, we specify the procedures of constructing our image processing pipeline. The pipeline is then tested using simulations in section 3. Section 4 describes our application to the SDSS DR7 data as well as the preliminary galaxy-galaxy lensing signals thereby measured. We summarize our results in section 5. Finally, we add some discussions about the systematic errors in galaxy-galaxy lensing measurement in Appendix B. All the data we show from this paper are available from the website: http://gax.shao.ac.cn/wtluo/weak_lensing/wl_sdss_dr7.tar.gz

2. IMAGE PROCESSING PIPELINE

The observed images of background galaxies are distorted by the foreground gravitational potential due to gravitational lensing. However, in order to use this information, the lensing distortion needs to be distinguished from other effects that can distort galaxy images. In particular, when light rays of galaxies go through the atmosphere, the lenses of a telescope and finally reach

the Couple-Charged Device (CCD) to be recorded, the images can be blurred or even distorted. The combined effects are usually described by the point spread function (PSF), which may change from position to position in a imaging field, and has to be corrected.

There are two types of distortions that can be caused by the PSF, one is an isotropic smearing of the original image and the other is an anisotropic effect which distorts the shape of an image. Our image processing pipeline is designed to correct for both effects. More specifically, we use BJ02 rounding kernel method for the anisotropic correction and the re-Gaussianization method of HS03 for isotropic correction. The reason for this combination is that the multiplicative error is the smallest among other methods (e.g. BJ02 method alone, re-Gaussianization method alone, and the KSB method) in our test using STEP2 data. The following is a more detailed description of our imaging processing method.

2.1. PSF anisotropy correction

The basic idea of the rounding kernel method of BJ02 to correct for PSF anisotropy effect is to convolve the PSF with a reconstructed kernel. In ideal case where the Fourier transformation of the kernel K is related to the PSF as $\tilde{K} = 1/\tilde{P}$ so that the convolution of K and P in real space is delta function, we have

$$I^o = P \otimes I^i, \quad (1)$$

$$K \otimes P = C(x), \quad (2)$$

where I^o is the observed image, I^i the intrinsic image, and K represents the reconstructed kernel [see Eqs. (7.1) - (7.4) in BJ02]. $C(x)$ is a circular 2D function without any anisotropy. In real applications, the PSF is not modeled perfectly, and we are seeking a kernel that can serve our purpose approximately. To this end, we expand the PSF with the QHO (Quantum Harmonic Oscillator) eigenfunctions,

$$P = \sum_{p,q} b_{pq} \phi_{pq}^\sigma(r, \theta), \quad (3)$$

$$K \otimes P = \sum_{p,q} b_{pq}^* \phi_{pq}^\sigma(r, \theta), \quad (4)$$

where

$$\phi_{pq}^\sigma(r, \theta) = \frac{(-1)^q}{\sqrt{\pi}\sigma^2} \sqrt{\frac{q!}{p!}} (r/\sigma)^m e^{im\theta} e^{-r^2/2\sigma^2} L_q^m(r^2/\sigma^2), \quad (5)$$

with L_q^m being the Laguerre polynomials, $m = p - q$ and σ is the size of the object in unit of pixels. If b_{pq}^* satisfies

$$b_{pq}^* = [(-1)^p / \sqrt{\pi}] \delta_{pq} \quad (6)$$

upto some order $N = p + q$, the PSF anisotropy is ideally removed. The detailed description is given in Appendix A.

2.2. PSF isotropy

PSF isotropic effect a.k.a smearing effect, dilutes the value of ellipticity and therefore leads to an underestimated shear. The method to correct for this effect we adopt here is re-Gaussianization method from HS03's.

The resolution factor \mathcal{R} is related to the size of the PSF and the galaxy images at the position of galaxy.

$$\mathcal{R} = 1 - \frac{T_p(1 - \beta_{22}^p)/(1 + \beta_{22}^p)}{T_g(1 - \beta_{22}^g)/(1 + \beta_{22}^g)}. \quad (7)$$

Higher order terms β_{22} is the ratio between b_{22} and b_{00} , which are the coefficients of QHO eigenfunctions. And T_p and T_g are the size of the PSF and galaxy respectively, estimated from the second moment $T = M_{xx} + M_{yy}$.

As pointed out in HS03, Eq. 7 (Eq. 14 in HS03) is only valid for the case that both PSF and galaxy images are Gaussian, which does not apply in real observations. HS03 fitted a Gaussian to the PSF, and then corrected the galaxy image for the effect of the residuals. After these treatments Eq. 7 is safe to be used. The process is called re-Gaussianization.

Suppose the Gaussian fit of the PSF $P(x)$ with second moment covariance matrix M_p is

$$G(x) = \frac{1}{2\pi\sqrt{\det M_p}} \exp\left(-\frac{1}{2}x^T M_p^{-1}x\right), \quad (8)$$

then the residual is the function of PSF subtracting this Gaussian fitting function,

$$\epsilon(x) = P(x) - G(x). \quad (9)$$

The galaxy image $I(x)$ then satisfy

$$I(x) = P \otimes f = G \otimes f + \epsilon \otimes f, \quad (10)$$

where f is the intrinsic brightness distribution of the galaxy. It can also be approximated with a Gaussian with second moments matrix of the galaxy image M_g ,

$$f^0 = \frac{1}{2\pi\sqrt{\det M_g}} \exp\left(-\frac{1}{2}x^T M_g^{-1}x\right), \quad (11)$$

where $M_g = M_I - M_p$ denotes the subtraction of second moments of the Gaussian fit of the PSF $G(x)$ from the galaxy second moments. Then the corrected image of the residual between PSF and Gaussian fit can be obtained using

$$I' = I - \epsilon \otimes f^0. \quad (12)$$

With all these treatments, the resolution factor can finally be obtained using Eq. 7 (see HS03 for more details). Based on the algorithms listed above, we constructed the image processing pipeline for our weak lensing studies.

3. TESTING THE PIPELINE WITH SIMULATIONS

Before applying our pipeline to real data, we first test it using simulated images that contain input shear signal as well as observational effects, such as PSF, sky background noise and pixellization. The two simulations used here are SHERA (SHEar Reconvolution Analysis) developed by M12, and GREAT3 as described in (Mandelbaum et al. 2014).

3.1. Testing with SHERA

3.1.1. SHERA data

SHERA M12 is designed to test the accuracy of shape measurement pipelines performing on ground-based images. It uses COSMOS (Cosmological Evolution Survey)

images as input, and the output are low-resolution images expected from a given ground-based observation. Here we set parameters, such as pixel size, PSF size, and sky background, according to SDSS. The weak lensing shear signal is added to each image using the following equation,

$$\begin{pmatrix} x^u \\ y^u \end{pmatrix} = \begin{pmatrix} 1 - \kappa - \gamma_1 & -\gamma_2 \\ -\gamma_2 & 1 - \kappa + \gamma_1 \end{pmatrix} \begin{pmatrix} x^l \\ y^l \end{pmatrix}, \quad (13)$$

where $(x^u, y^u), (x^l, y^l)$ are the un-lensed coordinates and lensed coordinates, respectively. The input shear (γ_1, γ_2) , are randomly generated ranging from -0.05 to 0.05.

The input galaxy image catalog is constructed from COSMOS ACS field (Koekemoer et al. 2007; Scoville et al. 2007a,b) following the method described in Leauthaud et al. (2007). The survey field is a 1.64 square degree region centered at 10:00:28.6+0.12:12:21.0 (J2000). The images are corrected for charge transfer inefficiency (Massey et al. 2010, CTI), geometric distortion, sky subtraction and cosmic ray, and further dithered using multi-drizzle algorithm. The final production has a co-added image of 7000×7000 pixels with a scale of $0.03''/\text{pixel}$. Further cuts are applied to fulfill the special requirements of SHERA as described in §4.1 of M12.

With the above criteria, 30,225 galaxies are selected. To mimic the SDSS images, additional galaxies are discarded either because these sources are undetectable in SDSS or because their sizes are smaller than the SDSS PSF, as detailed in M12. The final sample contains 26,113 galaxies.

3.1.2. PSF matching

The high resolution images obtained above are transformed into low resolution ones by PSF matching, i.e. by first de-convolving the images with the space PSF and then convolving them with the ground-based PSF. In Fourier space, this is mathematically given by

$$\tilde{I}^g = \frac{\tilde{G}^g}{\tilde{G}^s} \tilde{I}^s, \quad (14)$$

where I^g and G^g are the ground-based brightness distribution and PSF, whereas I^s and G^s are the corresponding space-based quantities. This PSF matching works as long as the power spectrum of the space PSF is larger than that of the ground PSF at all k ; otherwise it leads to ringing effect in the new image. As shown in Fig. 2 of M12, the power of SDSS PSF is smaller than that of COSMOS at all wave numbers, and so the PSF matching can be done safely.

In addition to the PSF, the noise level at the position of COSMOS in the SDSS imaging should also be taken into account. Fig. 1 shows the COSMOS image of a typical disk galaxy (left), SHERA simulated SDSS image (middle) and the real SDSS fpAtlas image (right) of the same galaxy. The bulge and disk components can be clearly identified from the original COSMOS image, whereas in SDSS only a bunch of pixels brighter than the detection limit (22.0 in r band) can be identified. We downgrade the high resolution COSMOS images to low resolution SDSS images. During this process, we miss 2.2 percent

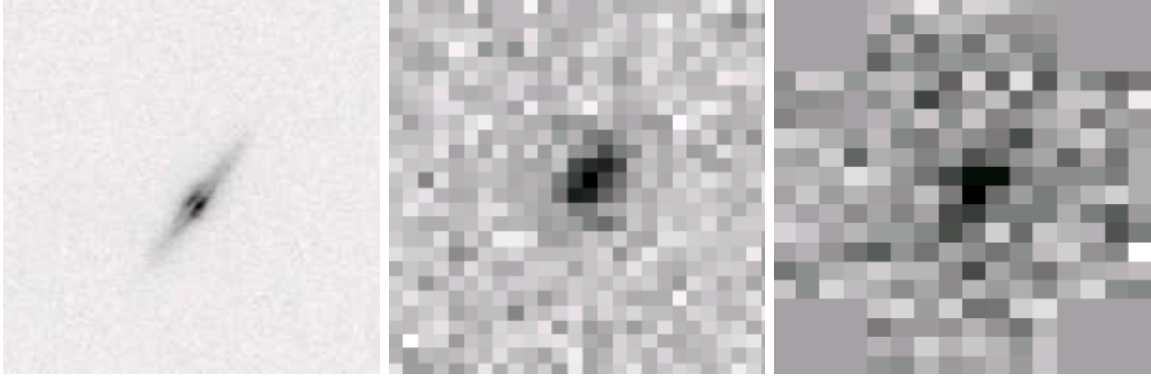


FIG. 1.— COSMOS image (left panel), SHERA simulated image (middle panel) and SDSS real image of the same galaxy (right panel).

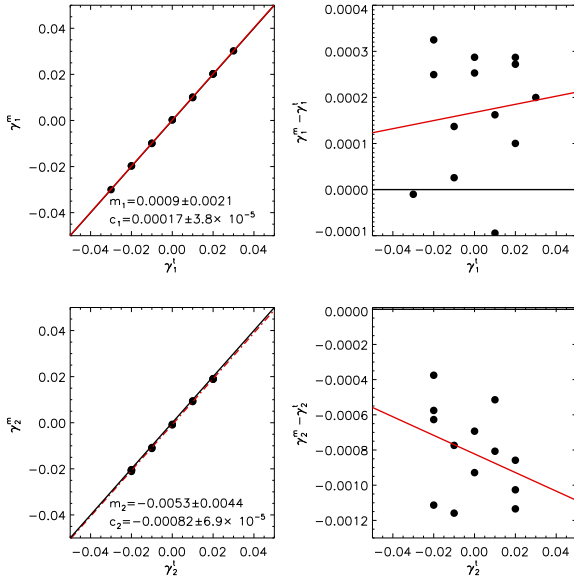


FIG. 2.— The correlation between the true (input) and measured shear components γ_1 (upper left) and γ_2 (lower left). The corresponding residuals versus the input values are plotted in the right two panels. The red lines are linear fitting results.

of the objects because of masking, which leaves a total of 25,527 images.

3.1.3. SHERA testing results

Using the mock SDSS images obtained above, we follow M12 to rotate each image 90 degree to eliminate the effect from intrinsic shape of galaxies. Here, in order to have a fair comparisons with the results of 12, the sky background and Poisson noise are not added to the simulation, so as to single out the performance of the PSF correction. Due to the size cut, only about 11,700 (44%) galaxies are selected for the final shear measurement.

To quantify the performance of the pipeline, we measure the shear, γ , in a given direction by averaging the shape of the source galaxies

$$\gamma = \frac{1}{2R} \frac{\sum w_i e}{\sum w_i}, \quad (15)$$

where $e = (e_1, e_2)$ describes the image shape, w_i is a weight assigned to an image, and R is the so called responsively calculated variance of the shape $R = 1 - \langle e^2 \rangle$.

The shape parameters, e_1 and e_2 , are obtained from the luminosity-weighted second moment of the 2-dimensional galaxy image (Kaiser et al. 1995),

$$M_{ij} = \frac{\sum G(x, y) I(x, y) (x - x_0)(y - y_0)}{\sum G(x, y) I(x, y)}, \quad (16)$$

where $I(x, y)$ is the brightness at a certain pixel located at (x, y) , and $G(x, y)$ is a kernel to smooth the image. Following convention, the ellipticities, e_1 and e_2 , are defined to be compressions along a fiducial direction (e.g. x) and along a direction that is at 45 degree with respect to the fiducial direction, respectively. The weight w_i for each galaxy is modeled as

$$w = \frac{1}{\sigma_e^2 + \sigma_{\text{sky}}^2}, \quad (17)$$

where σ_e is the variance of shape noise, and σ_{sky} describes the measurement error caused by the sky background and Poisson noise of photons.

We measured the two shear components $\gamma_1^{\text{measure}}$ and $\gamma_2^{\text{measure}}$, and Fig. 2 shows the correlation between the measured signal and input signal. The upper-left and lower-left panels are the one correlations for the two components, while the right panels are the corresponding residuals plotted against the input signal. The red lines are the linear fit to the data points. We use the standard terminology of multiplicative error (including PSF smearing effect and other unknown bias due to measurement method itself) and additive error (mostly from PSF ellipticity a.k.a PSF anisotropy) to connect the input signal and the measured signal:

$$\gamma_i^{\text{measure}} = (1 + m_i) \gamma_i^{\text{input}} + c_i \quad (i = 1, 2) \quad (18)$$

where m_i and c_i represent the two types of errors. In general, our pipeline achieves $< 1\%$ in the multiplicative error, with $m_1 = 0.09\% \pm 0.0021$ and $m_2 = 0.53\% \pm 0.0044$, and $< 0.1\%$ in the additive error, with $c_1 = 0.00017 \pm 3.8 \times 10^{-5}$ and $c_2 = 0.00082 \pm 6.9 \times 10^{-5}$. The fact that the multiplicative error in γ_2 is larger than that in γ_1 is due to pixellization. In Mandelbaum et al. (2012) the corresponding multiplicative errors are $m_1 = -1.6\% \pm 0.001$ and $m_2 = -2.7\% \pm 0.001$, and the additive errors are $c_1 = 0.00028 \pm 1.0 \times 10^{-5}$ and $c_2 = -0.00011 \pm 1.0 \times 10^{-5}$. The performance of our pipeline compares favorably to theirs.

However, we did find some shortcomings in our pipeline. When strong sky background and Poisson

noise are added, our pipeline sometimes suffers from non-convergence problem either during the calculation of the adaptive moments or in the estimation of the coefficients in Eq. A15. Thus, our pipeline cannot provide shape measurements for images with too low qualities. This reduces the number of sources that can be used for lensing studies. Due to the fact that the COSMOS image sample is small, we do not perform further test with noise as in M12. The convergence problem is also not discussed in this work, because it is difficult to examine whether it is from the iteration of adaptive moments or in the procedure when constraining the k_{ij} .

Nevertheless, as we will show in next subsection, even with the reduced number of sources, our pipeline provides lensing signals that are competitive in comparison to other pipelines.

3.2. GREAT3

GREAT3 (GRavitational lEnsing Accuracy Test 03) (Mandelbaum et al. 2014) is a successive testing project after STEP (Shear TEsting Program, Heymans et al. 2005), STEP2 (Massey et al. 2007a), GREAT08 (Bridle et al. 2009), and GREAT10 (Kitching et al. 2010), all of which are designed to compare the performances of different shape measurement methods in different observational conditions. From STEP to GREAT3, different PSFs, pixel sizes, galaxy morphologies are adopted. In particular, GREAT3 uses controlled galaxy morphologies generated with Shapelets (Refregier 2003), real galaxy morphologies obtained from COSMOS, co-added multiply observed images, variable PSF, and variable shears. Five major branches of simulations are generated using GalSim (Rowe et al. 2015): (i) a controlled sample generated with parametric (single or double Sersic) galaxy models; (ii) real galaxy sample with realistic morphology from HST COMOS dataset; (iii) multiple-epoch sample containing six images combined by dithering; (iv) sample with variable PSF that is reconstructed from star images; (v) a sample that includes all the above procedures. Each branch has ground versus space, and constant versus variable shear sub-branches.

For the constant shear datasets, 10,000 galaxies with shear are simulated. In order to cancel the effect of galaxy intrinsic shape, GREAT3 applies the rotation method as in the STEP2 simulation (Massey et al. 2007a). The basic idea is to use the fact that the shape is a spin-two quantity for which the sum of the original ellipticity with that of the 90-degree rotation is zero.

Our pipeline participated in the controlled ground constant, controlled space constant, real ground constant and real space constant tests. Overall, our pipeline ranks 15 among a total of 26 pipelines. As mentioned earlier, our pipeline suffers from non-convergence problem. Together with the size cut using the resolution factor in Eq. (7), only about 40% galaxies are used in the competition. Among our submissions, we found that the best weighting for our pipeline is to take the inverse of the shape noise and errors from ellipticity as in Mandelbaum et al. (2015, hereafter M05). The more detailed information and results about the GREAT3 competition can be found in M05.

4. APPLICATION TO THE SDSS DR7

After the above tests, we processed the SDSS DR7 (Abazajian et al. 2009) r band imaging data with our pipeline. The SDSS (York et al. 2000) consists of three imaging and spectroscopic surveys (Legacy, SEGUE, and Supernova), using a 2.5m telescope at Apache Point Observatory in Southern New Mexico. The SDSS photometric camera has two TDI (Time-Delay-and-Integrate) CCD scanning arrays (Gunn et al. 1998). One is a 6×5 CCD array, with each of the CCD having 2048×2048 pixels ($24 \mu\text{m} \approx 3 \text{arcseconds}$ on the sky) for five-band photometry, and the other is a $24 \times 2048 \times 400$ CCD array used for astrometry and focus monitoring. The DR7 imaging data, with u, g, r, i, z band information, covers about 8423 square degrees of the LEGACY sky, with information for about 230 million distinct photometric objects, and about 3240 square degrees of SEGUE sky, with about 127 million distinct objects (including many stars at low latitude). The total number of objects identified as galaxies is about 150 million.

TABLE 1

THIS TABLE LISTS THE SIX LENS SAMPLES WE SELECTED AND THE CORRESPONDING NUMBERS LISTED IN MANDELBAUM ET AL. (2005)

Sample	M_r	N_{gal}	N_{M05}	$\langle z \rangle$	$\sigma(z)$	$\langle L \rangle / L_*$
L1	$(-18, -17]$	18 614	6 524	0.029	0.007	0.071
L2	$(-19, -18]$	47 795	19 192	0.044	0.012	0.181
L3	$(-20, -19]$	138 988	58 848	0.069	0.020	0.450
L4	$(-21, -20]$	249 906	104 752	0.103	0.030	1.082
L5	$(-22, -21]$	164 653	63 794	0.140	0.038	2.364
L6	$(-23, -22]$	11 453	6 499	0.150	0.037	5.146

TABLE 2

THIS TABLE LISTS SOME PROPERTIES OF THE COLOR DIVIDED SUB-SAMPLES.

Sample	N_{gal}	$\langle z \rangle$	$\sigma(z)$	$\langle L \rangle / L_*$
L1R	5 383	0.030	0.007	0.073
L1B	13 231	0.029	0.007	0.071
L2R	17 471	0.045	0.013	0.186
L2B	30 324	0.044	0.012	0.179
L3R	67 058	0.069	0.019	0.459
L3B	71 930	0.069	0.019	0.443
L4R	138 316	0.102	0.030	1.092
L4B	111 590	0.104	0.030	1.072
L5R	98 808	0.141	0.038	2.378
L5B	65 845	0.138	0.038	2.347
L6R	6 880	0.155	0.034	5.130
L6B	4 573	0.141	0.037	5.182

4.1. Lens galaxies

In modern galaxy formation paradigm, brighter or more massive galaxies are believed to reside on average in more massive halos. This suggests that the galaxy-galaxy lensing signals should vary with the luminosity or stellar mass of lens galaxies, in that brighter or more massive lens galaxy sample should give higher lensing signal. This expectation has been proved to be correct, as shown in e.g. M05, M06 and Sheldon et al. (2009). In M05, lens galaxies in SDSS DR4 are divided into six luminosity samples, with the luminosity bins as given in Table. 1. Here we use the same luminosity bins. We select

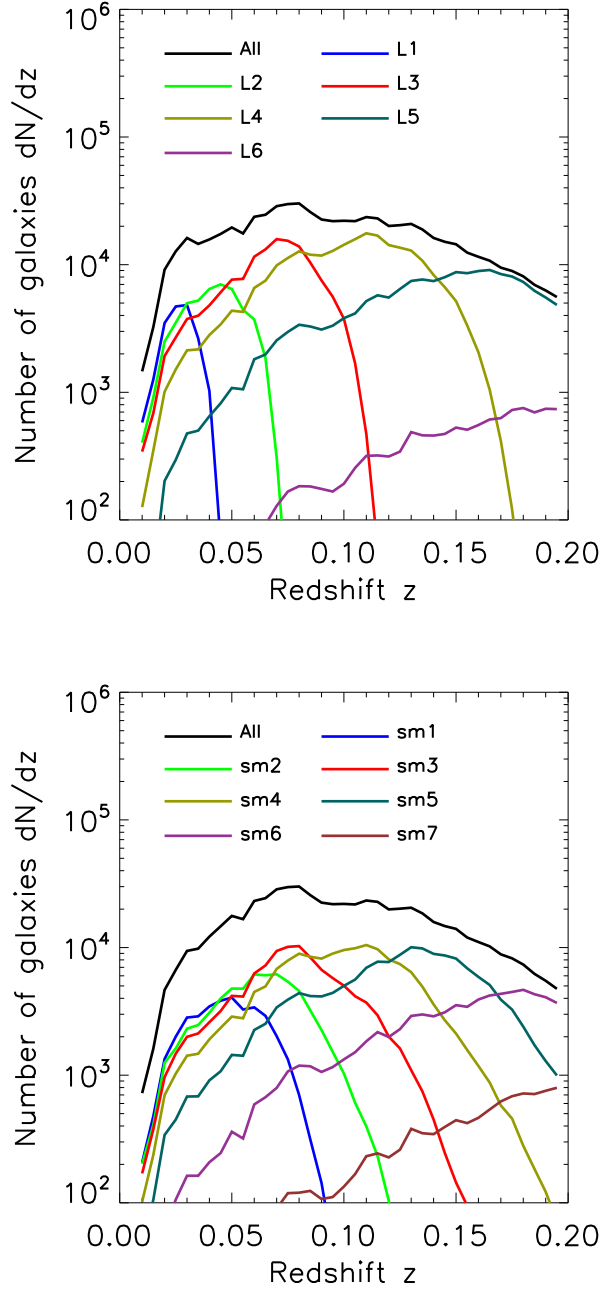


FIG. 3.— The redshift distribution of lens samples binned in luminosity (upper panel), and in stellar mass (lower panel).

lens samples from the New York University Value-Added Galaxy catalog (Blanton et al. 2005, NYU-VAGC) constructed from SDSS DR7 (Abazajian et al. 2009). All galaxies have been extinction-corrected, with apparent magnitude brighter than $r = 17.72$, with redshifts in the range $0.01 \leq z \leq 0.2$, and with spectroscopic redshift completeness $C_z > 0.7$. The completeness C_z is defined as the average percentage of the galaxies that have spectroscopic redshift in their local sky coverage. The resulting galaxy sample contains a total of 639,359 galaxies in a sky coverage of 7,748 square degrees.

The selection criteria and galaxy numbers of our six

TABLE 3

THIS TABLE LISTS THE SEVEN LENS SAMPLES WE SELECTED BINNED IN STELLAR MASS AND THE CORRESPONDING NUMBERS LISTED IN MANDELBAUM ET AL. (2006, HEREFTER M06). HERE AND HEREFTER M_* IS PRESENTED IN UNIT OF $h^{-2}M_\odot$.

Sample	$\log(M_*)$	N_{gal}	N_{M06}	$\langle z \rangle$	$\sigma(z)$	$\langle \log(M_*) \rangle$
sm1	[9.38, 9.69]	35 269	23 474	0.029	0.007	9.55
sm2	[9.69, 9.99]	62 742	40 952	0.044	0.012	9.85
sm3	[9.99, 10.29]	107 707	66 503	0.069	0.020	10.15
sm4	[10.29, 10.59]	153 787	90 019	0.103	0.030	10.45
sm5	[10.59, 10.89]	155 242	82 734	0.140	0.038	10.73
sm6	[10.89, 11.20]	73 048	39 729	0.150	0.037	11.01
sm7	[11.20, 11.50]	9 807	8 096	0.150	0.037	11.29

TABLE 4

THIS TABLE LISTS THE SUB SAMPLES BINNED IN STELLAR MASS AND SPLIT INTO RED AND BLUE.

Sample	N_{gal}	$\langle z \rangle$	$\sigma(z)$	$\langle \log(M_*) \rangle$
sm1r	7 447	0.038	0.010	9.56
sm1b	27 522	0.054	0.016	9.55
sm2r	19 604	0.051	0.015	9.87
sm2b	43 138	0.070	0.020	9.85
sm3r	48 669	0.069	0.019	10.16
sm3b	59 038	0.089	0.026	10.15
sm4r	85 839	0.090	0.025	10.45
sm4b	67 948	0.113	0.032	10.44
sm5r	102 360	0.120	0.036	10.74
sm5b	52 882	0.136	0.037	10.72
sm6r	57 063	0.149	0.037	11.01
sm6b	15 985	0.146	0.038	10.99
sm7r	8224	0.158	0.034	11.29

TABLE 5

THIS TABLE LISTS THE SUB SAMPLES BINNED IN STELLAR MASS AND SPLIT INTO STAR FORMING GALAXIES AND QUENCHED GALAXIES.

Sample	N_{gal}	$\langle z \rangle$	$\sigma(z)$	$\langle \log(M_*) \rangle$
sm1sf	29 460	0.053	0.016	9.55
sm1qu	5 809	0.038	0.011	9.56
sm2sf	46 544	0.068	0.020	9.85
sm2qu	16 198	0.051	0.016	9.87
sm3sf	66 138	0.086	0.027	10.15
sm3qu	41 569	0.069	0.019	10.16
sm4sf	73 606	0.109	0.031	10.44
sm4qu	80 181	0.090	0.026	10.45
sm5sf	50 107	0.137	0.034	10.72
sm5qu	105 135	0.119	0.034	10.74
sm6sf	11 151	0.157	0.033	10.98
sm6qu	61 897	0.147	0.038	11.01
sm7qu	8 219	0.157	0.034	11.29

lens galaxy samples are listed in Table. 1. The scatter of the redshift distribution, the ratio between the mean luminosity and the characteristic luminosity L_* ($M_* = -20.44$, as given in Blanton et al. (2003)), and the number galaxies contained in each sample are also listed in Table. 1. On average, the number of galaxies in our sample is 2 to 3 time larger than the corresponding M05 sample, simply because DR7 covers a larger area than DR4 (7748 v.s. 4783 square degrees). The mean redshift from our lens sample is slightly lower than that of M05, because M05 also used lenses at $z > 0.2$ while

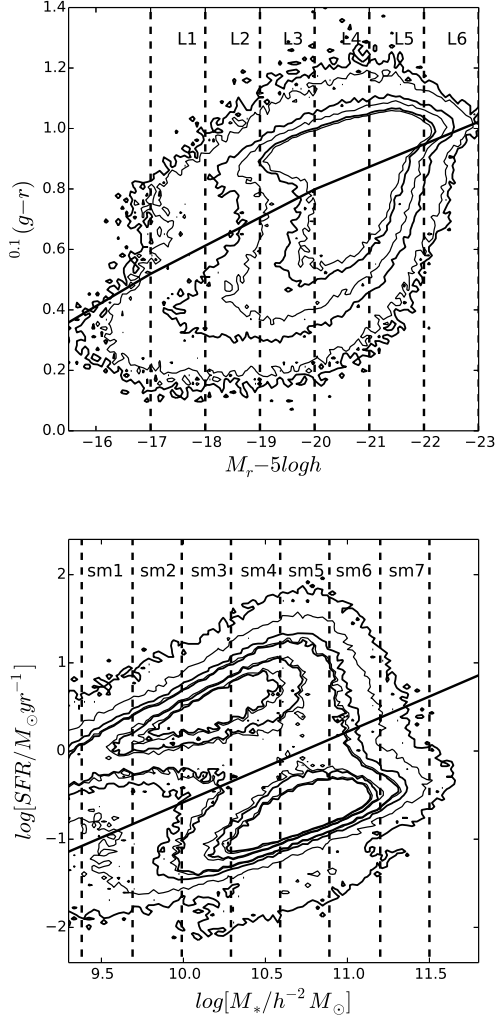


FIG. 4.— Upper panel: The distribution of lens galaxies in the color-absolute magnitude plane as represented contours. The luminosity bins used in the paper are shown as vertical dashed lines. The solid line is the function used to divide red and blue galaxies (Yang et al. 2008). Lower Panel: The distribution of lens galaxies in the star formation Rate (SFR)-stellar mass plane as represented by contours. The stellar mass bins used in the paper are shown as vertical lines and the solid line is the function separating star forming galaxies from quenched galaxies (Luo et al. 2014).

the redshift range of our sample is between 0.01 and 0.2. The redshift distributions of our lens samples are shown in Fig. 3. The solid black line is for the total sample, while the colored lines are for the six luminosity samples, as indicated.

We further divide galaxies in each luminosity bin into blue and red according to

$$0.1(g-r) = 1.022 - 0.0652x - 0.0031x^2, \quad (19)$$

where $x = 0.1M_r - 5 \log h + 23.0$ (Yang et al. 2008). The upper panel of Fig. 4 shows the distribution of the lens galaxies in the color-absolute magnitude plane, with the black dashed line showing the demarcation line (Eq. 19), and the vertical lines marking the different luminosity bins we use.

In Mandelbaum et al. (2006, hereafter M06), galaxy-galaxy lensing signals are measured for lens galaxies

binned in stellar masses. Here we make a similar analysis. Note, however, that the stellar masses in M06 are estimated from spectra, as described in Kauffmann et al. (2003), while the stellar masses in our sample are estimated using the model described in Bell et al. (2003). Table 3 lists some of the properties in different stellar mass bins, such as the number of galaxies in our samples in comparison to that in M06, the mean redshift, the scatter in redshift, and the mean stellar mass. We further divide galaxies in each stellar mass bin into red and blue samples using Eq. (19). Table 4 shows the number, mean redshift, scatter of the redshift, and the mean stellar mass of the galaxies in each of the color samples. In general, the mean stellar mass of the red sample is larger than that of the corresponding blue sample by 0.01 to 0.02 dex.

In addition to the color separation, we also separate galaxies in different stellar mass bins into star forming and quenched subsamples. Here we use the Yang et al. (2013); Luo et al. (2014) scheme to define star forming and quenched galaxies, and the dividing line is defined to be

$$\log SFR = (\log M_* - 2 \log h - 11.0) \times 0.8. \quad (20)$$

The lower panel of the Fig. 4 shows the distribution of galaxies in the SFR - stellar mass plane, with the black dashed line showing the dividing line given above. Note that M_* is presented in units of $h^{-2}M_\odot$. Table 5 lists the number, the mean redshift, the scatter of the redshift, and the mean stellar mass of each subsample. For each mass bin, the average stellar masses in the two subsamples are similar, while the mean redshifts differ slightly in that a quenched sample has slightly higher mean redshift than the star forming sample.

4.2. Source galaxies

Following Mandelbaum et al. (2005, hereafter M05), we only chose galaxies defined as OBJC_TYPE=3 from PHOTO pipe developed by Lupton et al. (2001). They have to be detected both in r and i bands (with $r < 22$ and $i < 21.6$ in model magnitudes). We firstly create a preliminary catalog (Cat I) from SDSS casjobs with 115,052,555 galaxies containing positions (including run, rerun, camcol, field, obj, ra, dec), and photometric redshifts.

Then we process the Cat I to include more information such as, (i) sky level in unit of photon-electron using the information of gain value in r band, (ii) the position of each galaxy in terms of CCD coordinates in order to get the PSF from psField files, (iii) the SPA value denoting the angle between the camera column position with respect to north from fpC files. We define this catalog as Cat II containing 91,941,657 galaxies. The missing 23,110,898 are caused by the fact that we discard objects with -9999 value on zero-point, extinction coefficient, airmass, sky in r band, and only keep galaxies with flags BINNED1 (detected at ≥ 5), SATURATED=0 (do not have saturated pixels), EDGE=0 (do not locate at the edge of the CCD), MAYBE-CR=0 (not cosmic rays), MAYBE-EGHOST=0 (not electronic ghost line) and PEAKCETER=0 (centroiding algorithm works well for this object).

Then we use our pipeline to process the images from fpAtlas and psField files to generate the final catalog

(Cat III). Cat III contains the information of position, redshift, ellipticity, resolution factor and calibration errors of each galaxy. The errors are estimated from both sky background and photon noise as described by Eq. 11 and Eq. 12 in M05. We only keep objects with valid e_1 , e_2 , resolution factor. As mentioned above, our pipeline will abandon those galaxy images that have inconvergent values of ellipticity. From GREAT3 testing, about 40% galaxies were excluded due to this effect, and we further require that $\mathcal{R} > 1/3$ which tosses another 10%-30% (varies depending on different simulation sets.) or so. Here, our Cat III has a final number of galaxies of 41,631,361, which is $\sim 45\%$ of the original Cat II. The Irregularity image from SDSS photo-pipe ($\sim 4\%$), resolution cut ($\sim 11\%$), and inconvergence problem ($\sim 40\%$) together reduce the number of the final catalog by $\sim 55\%$.

4.3. Galaxy-galaxy lensing signals

From weak lensing shear measurements, we can estimate the excess surface density (ESD) of the lens system, which is defined as,

$$\Delta\Sigma(R) = \Sigma(\leq R) - \Sigma(R), \quad (21)$$

where $\Sigma(\leq R)$ and $\Sigma(R)$ are the mean surface mass density inside a certain radius R and at the radius R , respectively. The tangential shear is related to this quantity via a critical density,

$$\gamma_t(R)\Sigma_c = \Delta\Sigma(R), \quad (22)$$

where the critical density in a lensing system is,

$$\Sigma_c^{-1} = \frac{4\pi G}{c^2} \frac{D_l D_{ls} (1+z_l)^2}{D_s}. \quad (23)$$

Here D_s , D_l and D_{ls} are the angular diameter distances of the source, the lens and between the lens and the source, respectively.

The mean excess surface density around a lens galaxy is specified by the line-of-sight projection of the galaxy-matter cross correlation function, $\xi_{gm}(r)$, so that

$$\Sigma(R) = 2\bar{\rho} \int_R^\infty \xi_{gm}(r) \frac{r dr}{\sqrt{r^2 - R^2}}, \quad (24)$$

and

$$\Sigma(\leq R) = \frac{4\bar{\rho}}{R^2} \int_0^R y dy \int_y^\infty \xi_{gm}(r) \frac{r dr}{\sqrt{r^2 - y^2}} \quad (25)$$

with $\bar{\rho}$ the average background density of the Universe. Note in both equations, we have omitted the contribution from the mean density of the universe, as it does not contribute to the ESD.

If taking photometric redshift error of source galaxies into account, then it has to convolve with the error distribution (see M05),

$$\Sigma_c^{-1}(z_l, z_p) = \int p(z_s|z_p) \Sigma_c^{-1}(z_l, z_s) dz_s, \quad (26)$$

where z_l , z_p , z_s denote the spectroscopic redshift of the lens galaxy, the photometric redshift of the source galaxy and the spectroscopic redshift of the source galaxy. Because the spectroscopic redshift of most of the source galaxies are not available, the determination of $p(z_s|z_p)$

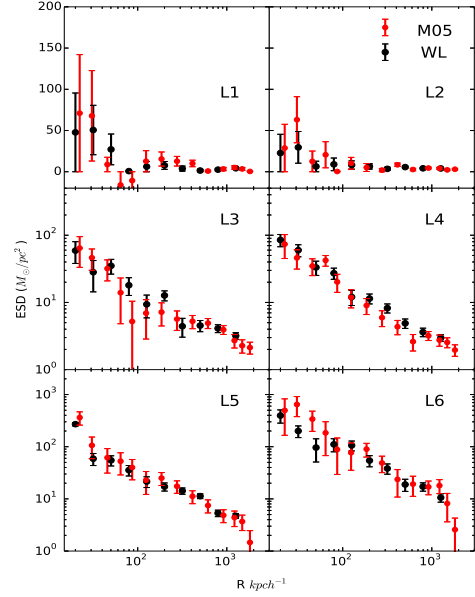


FIG. 5.— The excess surface density (ESD) of our lens galaxies in six luminosity bins. The black dots are our measurements and the red dots are results obtained by M05.

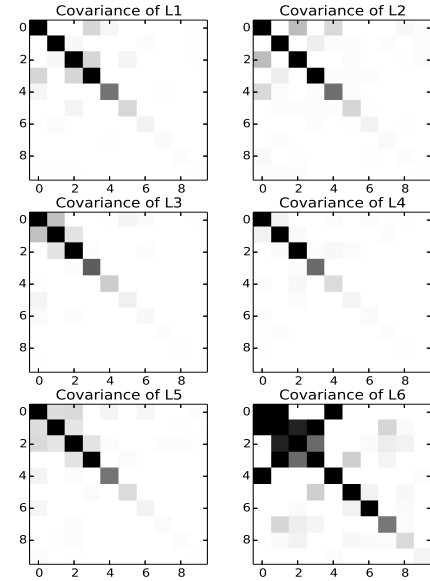


FIG. 6.— The covariance matrix of the data points for our six luminosity bins. The grey scale color has been re-scaled so that smaller values can be reflected on this covariance map. The values of the covariance map are provided in extra files.

relies on other spectroscopic surveys. In M05's results, they obtain the error distribution by cross identify the subsample of their source galaxies with other spectroscopic surveys such as DEEP2, COMBO-17.

Fig. 5 shows the average excess surface density of our lens galaxies divided into six luminosity bins. The black

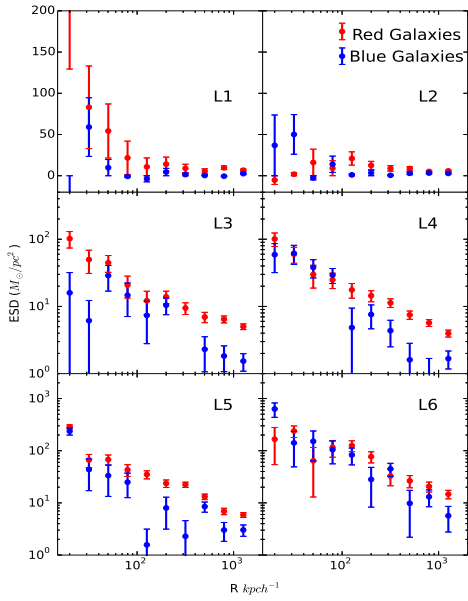


FIG. 7.— The ESDs for red (red dots) and blue (blue dots) galaxies in different luminosity bins.

dots are our measurements and the red dots are kindly provided by Rachel Mandelbaum. For simplicity we calculate the signals around each galaxy sample in 10 equal logarithmic bins rather than 45 bins and re-bin the signal as in M05. The error bars are estimated from 2500 bootstrap resampling of the lens galaxies. Thus the related error bars shown in the figure are mainly from the sampling variance. The covariance matrix of the data points shown in Fig. 5 are given in Fig. 6. We rescaled the color so that smaller values can be seen. For those who are interested, the covariance values can be obtained via the link provided at the end of section 1.

Following M05, we give a detailed list of possible systematic errors that the measured signals might have in Appendix B. The total 2σ systematic error in $\delta\gamma/\gamma$ is about $[-9.1\%, 20.8\%]$, slightly larger than those quoted in M05 at about $[-9.0\%, +18.4\%]$ due to the fact that we directly use the value from M05 of sample with $r > 21.0$ to estimate the systematic. In addition, the redshift tests and γ_{45} component tests are consistent with zero. Overall, our results are in very good agreement with M05 ones with smaller error bars, which is due to the larger number of lens galaxies in our samples. Both signals show clear increasing trend as the luminosity increases.

For each of our luminosity bin, we have divided galaxies into red and blue subsamples, we show the corresponding galaxy-galaxy lensing signals in Fig. 7. The error bars become larger due to the decreased number of lens galaxies in the subsamples. For very faint lens galaxies in L1 bin, the red galaxies have larger ESDs than blue galaxies especially at small radius, indicating that red galaxies on average locate in relatively more massive halos than their blue counterparts. For relatively bright galaxies, especially in L2-L4 bins, the red galaxies show similar ESDs as blue ones at small scales, while at larger scales with $R > 200 h^{-1}\text{kpc}$, the signals from red galaxies are

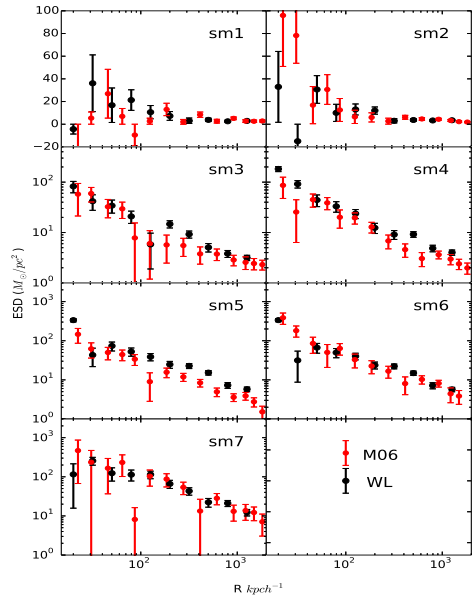


FIG. 8.— The ESDs for lens galaxies that are separated into different stellar mass bins. Here in each panel we compare the results between our sample (black dots) and M06 (red dots).

much larger than the blue galaxies. The much more enhanced ESDs for red galaxies at large scale indicate that these galaxies may locate in or near massive host halos.

Next, we proceed to estimate the ESDs for galaxies that are separated into different stellar mass bins. Shown in Fig. 8, the black dots are our measurements and the red dots are those obtained by M06. Similar to the luminosity separation, our results agree with those of M06 very well, except in the sm5 bin where ours show enhanced ESDs at radius $1500 > R > 200 h^{-1}\text{kpc}$. This enhancement indicate that the additional galaxies in this sample relative to M06 may have a larger portion in or near massive halos.

To be complete, we also measure the ESDs for our color and star formation subsamples in different stellar mass bins. Shown in Fig. 9 are the results for red and blue galaxies. The color dependences in different stellar mass bins are quite similar to those in different luminosity bins. In addition, as the color are closely related with the newly formed stars, i.e. young galaxies are bluer whereas old galaxies are redder. Thus the results shown in Fig. 10 for star forming and quenched galaxies are similar to red galaxies.

Finally, as modelled in M05, the above measured ESD signals can be fitted to probe the average halo mass of the lens systems. Also as pointed out in Yang et al. (2006a), the central and satellite galaxies have very different lensing signals, we differ a more detailed modeling of the ESDs on these lens galaxies in a subsequent paper by separating them into central and satellite galaxies.

5. DISCUSSION AND CONCLUSION

In weak lensing studies, to obtain a reliable measurement of the lensing signals requires high accuracy of image processing. In this paper, we build our image processing pipeline to achieve accurate shape measurement

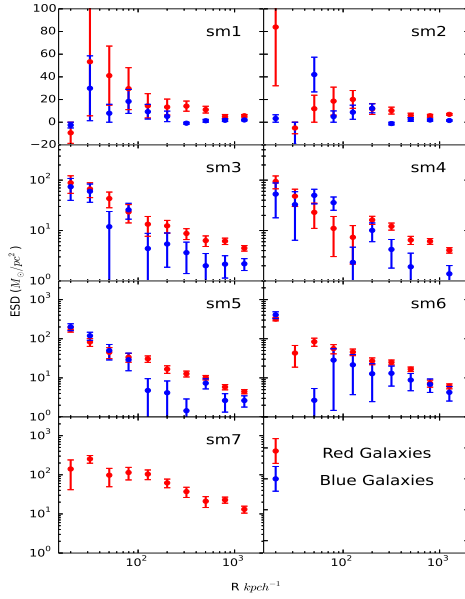


FIG. 9.— The ESDs for red (red dots) and blue (blue dots) lens galaxies in different stellar mass bins.

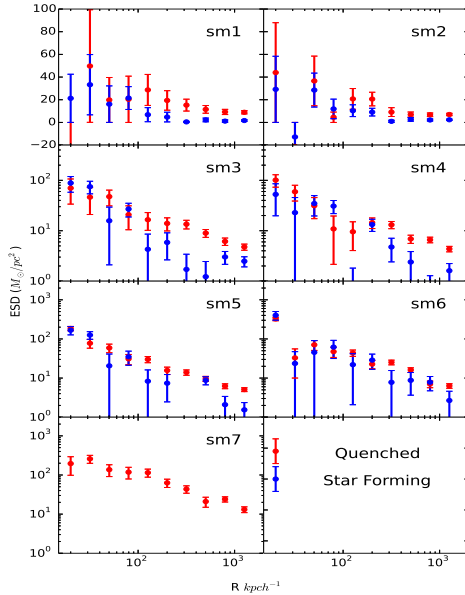


FIG. 10.— The ESDs for quenched (red dots) and star forming (blue dots) lens galaxies in different stellar mass bins.

for weak lensing study based on BJ02 and HS03 method. The basic performance of our pipeline is summarized as follows.

- This pipeline is tested using SHERA and GREAT3 simulations. Tests show that our pipeline works well on PSF correction in the absence of sky background noise, the corrected PSF multiplicative errors are far below 1% requirements (0.009% for γ_1

and -0.053% for γ_2) for PSF correction only.

- For more realistic simulations with sky background noise, our pipeline skips about 40% galaxies that might caused by the inconvergence problem of the method. In addition, to have a sufficient image resolution $\mathcal{R} > 1/3$ will remove additional 30% galaxies. However, using the remaining galaxy images still helps us to obtain similar lensing reconstruction accuracy as most of the other methods as shown in GREAT3 results paper (Mandelbaum et al. 2015).
- We applied our pipeline to the SDSS DR7 r band imaging data and create a catalog containing 41,631,361 galaxies with the information of position, photometric redshift, ellipticity and ellipticity measurement error due to sky background and Poisson noise.
- Using these galaxy images, we calculated the galaxy-galaxy lensing signals around foreground lens galaxies binned in different luminosities and stellar mass ranges. Comparing to those of M05 and M06, our results show very good agreement with these previous studies with significantly reduced error bars. The systematic checks using γ_{45} components, redshift tests and random sample tests show null signals. These consistencies further confirmed the reliability of our pipeline.
- We have also separate the galaxies in different luminosity or stellar mass bins into red/blue or star forming/quenched subsamples. The galaxy-galaxy lensing signals show quite different scale dependence among these subsamples.

As this is the first paper in a series on galaxy-galaxy lensing studies, here we focused on testing the reliability of our image processing pipeline. In the upcoming work, we will use the shape catalog obtained from SDSS DR7 to study galaxy-galaxy lensing signals around galaxy groups obtained by Yang et al. (2007, 2012) by separating lens galaxies into central and satellite subsamples, etc.

On the other hand, as our pipeline can not make full use those images that suffered significantly from the strong noises, we intend to improve the pipeline by combining the Fourier space based method (Zhang et al. 2015). As pointed out in Zhang et al. (2015), the Fourier space based method is indeed very powerful in dealing with asymmetric systems and those images that are strongly suffered from the noise.

WL hereby thank Rachel Mandelbaum from Carnegie Mellon University for very useful guiding and discussions at various stages in carrying out this project and providing the data points presented in this paper, Dandan Xu from Heidelberg University for useful discussion. This work is supported by the 973 Program (No. 2015CB857002), NSFC (Nos. 11128306, 11121062, 11233005, 11503064), the Strategic Priority Research Program “The Emergence of Cosmological Structures” of the Chinese Academy of Sciences, Grant No. XDB09000000, and a key laboratory grant from

the Office of Science and Technology, Shanghai Municipal Government (No. 11DZ2260700) as well as Chinese Scholarship Council(201504910477) and Shanghai Natural Science Foundation, Grant No. 15ZR1446700. LF acknowledges support from NSFC grants 11103012 & 11333001 & Shanghai Research grant 13JC1404400.

LR acknowledges the NSFC(grant No.11303033), the support from Youth Innovation Promotion Association of CAS.

This work is also supported by the High Performance Computing Resource in the Core Facility for Advanced Research Computing at Shanghai Astronomical Observatory.

APPENDIX

A. BJ02 METHOD

In order to construct the basic components for K as well as the corresponding coefficients of individual components. Eqs. (7.18) - (7.22) in BJ02 list the 3×3 basic kernel components constructed on the basis of flux conservation. Flux conservation requires that the kernel is the sum of an identical matrix with the derivative matrices whose elements summation is zero. The continuous form of D is:

$$D_{ij} = \left(\frac{\partial}{\partial x} + i\frac{\partial}{\partial y}\right)^i \left(\frac{\partial}{\partial x} - i\frac{\partial}{\partial y}\right)^j \quad (\text{A1})$$

$$= \sigma^{-(i+j)} (a_q^{\sigma\downarrow} - a_p^{\sigma\uparrow})^i (a_p^{\sigma\downarrow} - a_q^{\sigma\uparrow})^j. \quad (\text{A2})$$

Here a_p^{\downarrow} and a_p^{\uparrow} are defined as lowering and raising operators for 2D QHO eigenfunctions, which have the properties

$$a_p^{\downarrow} = \frac{1}{2} \left[\frac{x - iy}{\sigma} + \sigma \left(\frac{\partial}{\partial x} - i\frac{\partial}{\partial y} \right) \right], \quad (\text{A3})$$

$$a_p^{\uparrow} = \frac{1}{2} \left[\frac{x + iy}{\sigma} - \sigma \left(\frac{\partial}{\partial x} + i\frac{\partial}{\partial y} \right) \right], \quad (\text{A4})$$

$$a_q^{\downarrow} = \frac{1}{2} \left[\frac{x + iy}{\sigma} + \sigma \left(\frac{\partial}{\partial x} + i\frac{\partial}{\partial y} \right) \right], \quad (\text{A5})$$

$$a_q^{\uparrow} = \frac{1}{2} \left[\frac{x - iy}{\sigma} - \sigma \left(\frac{\partial}{\partial x} - i\frac{\partial}{\partial y} \right) \right]. \quad (\text{A6})$$

The derivative along x and y axis can be treated as convolving a matrix with the image $I(x, y)$.

$$\frac{\partial I}{\partial x} = \begin{pmatrix} 0 & 0 & 0 \\ \frac{-1}{2} & 0 & \frac{1}{2} \\ 0 & 0 & 0 \end{pmatrix} \otimes I, \quad (\text{A7})$$

$$\frac{\partial I}{\partial y} = \begin{pmatrix} 0 & \frac{1}{2} & 0 \\ 0 & 0 & 0 \\ 0 & \frac{-1}{2} & 0 \end{pmatrix} \otimes I, \quad (\text{A8})$$

$$\frac{\partial^2 I}{\partial x^2} = \begin{pmatrix} 0 & 0 & 0 \\ 1 & -2 & 1 \\ 0 & 0 & 0 \end{pmatrix} \otimes I, \quad (\text{A9})$$

$$\frac{\partial^2 I}{\partial y^2} = \begin{pmatrix} 0 & 1 & 0 \\ 0 & -2 & 0 \\ 0 & 1 & 0 \end{pmatrix} \otimes I, \quad (\text{A10})$$

$$\frac{\partial^2 I}{\partial x \partial y} = \begin{pmatrix} \frac{-1}{4} & 0 & \frac{1}{4} \\ 0 & 0 & 0 \\ \frac{1}{4} & 0 & \frac{-1}{4} \end{pmatrix} \otimes I. \quad (\text{A11})$$

These are the components of the Second Derivative in the Gradient Direction(SDGD) filter in image edge detection.

In discrete form, the 3×3 basic kernel are:

$$D_{10} = \begin{pmatrix} 0 & i(1/2) & 0 \\ -1/2 & 0 & 1/2 \\ 0 & i(-1/2) & 0 \end{pmatrix}; D_{01} = \overline{D_{10}}, \quad (\text{A12})$$

$$D_{20} = \begin{pmatrix} i(-1/2) & -1 & i(1/2) \\ 1 & 0 & 1 \\ i(1/2) & -1 & i(-1/2) \end{pmatrix}; D_{02} = \overline{D_{20}}, \quad (\text{A13})$$

$$D_{11} = \begin{pmatrix} 0 & 1 & 0 \\ 1 & -4 & 1 \\ 0 & 1 & 0 \end{pmatrix}. \quad (\text{A14})$$

The D_{00} is the idential matrix. D_{11} is an actually Laplacian operator. They contains all the first and second order derivatives. Higher order derivatives can be found by convolving 3×3 components. Then the kernel bears the following form

$$K = \sum k_{ij} D_{ij}, \quad (\text{A15})$$

where k_{ij} are the coefficients satisfying $k_{ij} = \overline{k_{ij}}$ so that K is a real matrix rather than a complex one.

Combining equations 3 and A15 we have

$$\mathbf{b}^* = \sum_{ij} k_{ij} D_{ij} \mathbf{b}, \quad (\text{A16})$$

where $D_{ij} \mathbf{b}$ obeys the recursion:

$$D_{00} \mathbf{b} = \mathbf{b}, \quad (\text{A17})$$

$$D_{(i+1)j} \mathbf{b} = \frac{1}{\sigma} (a_q^\downarrow - a_p^\uparrow) D_{ij} \mathbf{b}, \quad (\text{A18})$$

$$D_{i(j+1)} \mathbf{b} = \frac{1}{\sigma} (a_p^\downarrow - a_q^\uparrow) D_{ij} \mathbf{b}. \quad (\text{A19})$$

The last step is to constrain the coefficients k_{ij} by setting \mathbf{b}^* to meet the requirements of

$$\mathbf{b}_{pq}^* = 0, (m = p - q = 2). \quad (\text{A20})$$

For the unspecified \mathbf{b}^* , a simple treatment of setting $k_{pq} = 0$ is easy yet satisfies all the requirements of \mathbf{b}^* .

For instance, if we take $N=4$ and then the coefficient matrix we used to constrain is

$$\mathbf{b}^* = \begin{pmatrix} b_{00}^* & b_{01}^* & b_{02}^* \\ b_{10}^* & b_{11}^* & b_{12}^* \\ b_{20}^* & b_{21}^* & b_{22}^* \end{pmatrix}. \quad (\text{A21})$$

In the ideal case, we have

$$\mathbf{b}^* = \begin{pmatrix} \frac{1}{\sqrt{\pi}} & 0 & 0 \\ 0 & -\frac{1}{\sqrt{\pi}} & 0 \\ 0 & 0 & \frac{1}{\sqrt{\pi}} \end{pmatrix}. \quad (\text{A22})$$

And b_{10}^* naturally goes to zero if the centroid of the PSF we measure is true, so this term does not have any constraining power to k_{ij} . So the left ones we use are simply $b_{00}^*, b_{11}^*, b_{20}^*$ and b_{22}^* .

Then the linear equation to calculate k_{ij} is

$$\begin{pmatrix} D_{00}b_{00} & D_{01}b_{00} & D_{02}b_{00} & D_{11}b_{00} \\ D_{00}b_{11} & D_{01}b_{11} & D_{02}b_{11} & D_{11}b_{11} \\ D_{00}b_{20} & D_{01}b_{20} & D_{02}b_{20} & D_{11}b_{20} \\ D_{00}b_{22} & D_{01}b_{22} & D_{02}b_{22} & D_{11}b_{22} \end{pmatrix} \begin{pmatrix} k_{00} \\ k_{10} \\ k_{02} \\ k_{11} \end{pmatrix} = \begin{pmatrix} b_{00}^* \\ b_{11}^* \\ b_{20}^* \\ b_{22}^* \end{pmatrix} = \begin{pmatrix} \frac{1}{\sqrt{\pi}} \\ -\frac{1}{\sqrt{\pi}} \\ 0 \\ \frac{1}{\sqrt{\pi}} \end{pmatrix} \quad (\text{A23})$$

And due to the fact that $k_{ij} = \overline{k_{ij}}$, the dimensions are shrinked dramatically by only considering k_{01} and k_{02} . Before solving this linear equation, we have to calculate each elements of the coefficient matrix. The $D_{ij} \mathbf{b}$, \mathbf{b} denotes all the entries of the coefficient vector when expanding the PSF image using elliptical Laguerre basis. A17 is valid for continuous function, but for pixelized data, $D_{ij} \mathbf{b}$ can be solved using BJ02 EQ.7.26,

$$D_{10} \mathbf{b} = \frac{1}{2} (T_{z1} \mathbf{b} - T_{-z1} \mathbf{b}) + \frac{1}{2} i (T_{z2} \mathbf{b} - T_{-z2} \mathbf{b}) \quad (\text{A24})$$

where $z1 = 1/\sigma$, $z2 = i/\sigma$. T_z is defined as the translation operator.

$$T_z f(x, y) = f(x - x0, y - y0), \quad (\text{A25})$$

$$z = (x0 + iy0)/\sigma. \quad (\text{A26})$$

So we have

$$T_{z1} f(x, y) = f(x - 1, y), \quad (\text{A27})$$

$$T_{z2} f(x, y) = f(x, y - 1). \quad (\text{A28})$$

The functional form of T_z can be derived from the decomposition of PSF image, i.e. $P = \sum b_{pq} \psi_{pq}^\sigma$ and $T_z P = \sum b'_{pq} \psi_{pq}^\sigma$. We denote \mathbf{b}' as the new coefficients after operation T_z

$$\mathbf{b}' = T_z \mathbf{b}, \quad (\text{A29})$$

$$b'_{p'q'} = \sum T_{p'q'}^{pq} b_{pq} \quad (\text{A30})$$

$$T_z \psi_{pq}^\sigma = \sum T_{p'q'}^{pq} \psi_{p'q'}^\sigma, \quad (\text{A31})$$

$$T_{p'q'}^{pq} = \sigma^2 \int d^2x (T_z \psi_{pq}^\sigma) \psi_{p'q'}^{\bar{\sigma}}. \quad (\text{A32})$$

This directly leads to the first term,

$$T_{00}^{00} = e^{-|z|^2/4}. \quad (\text{A33})$$

And the left terms can be also solved recursively with the following relation.

$$T_{p'q'}^{pq} = h(p, p') \bar{h}(q, q'), \quad (\text{A34})$$

$$h(p, 0) = \frac{(-z/2)^p}{\sqrt{p!}} e^{-|z|^2/8}, \quad (\text{A35})$$

$$h(p, p' + 1) = [\sqrt{p} h(p - 1, p') + \frac{1}{2} \bar{z} h(p, p')]/\sqrt{p' + 1}. \quad (\text{A36})$$

B. SYSTEMATIC CHECKS

Systematic errors

There are five major systematics in weak lensing measurement as described in HS03 and M05. Table. 6 listed these major biases in our work compared to M05. Below we give a brief introduction of each of them.

TABLE 6
THIS TABLE LISTS THE FIVE MAJOR SYSTEMATICS IN OUR WEAK LENSING MEASUREMENTS COMPARED TO M05.

Bias (per cent)	M05	this work
Selection bias	[0,10.3]	[0,12.3]
PSF reconstruction bias	± 2.1 to ± 2.4	± 2.2
PSF dilution bias	[-2.8,4.0]	*[-2.8,4.0]
Shear responsivity error	[0,1.7]	[0,2.3]
Noise rectification error	[-3.8,0]	[-4.08,0]
Total 2σ $\delta\gamma/\gamma$ (per cent)	[-9.0,18.4]	[-9.1,20.8]

Selection bias

The first selection bias is mainly caused by the asymmetries of the PSF, denoted as ‘PSF selection bias’ in Kaiser (2000), which selects more galaxies elongated in one direction than the ones elongated along another direction. Secondly, the shear introduce asymmetries in the same way as PSF, i.e. shear elongates galaxies along certain direction and hence makes galaxies with major axis aligned with that direction more easily detected. In HS03, this is named as ‘shear selection bias’. Finally, many significance based object detection methods preferentially select circular objects leading to underestimation of the shear signal. M05 gives an estimation of the selection bias to be [0,5.7]% for galaxies with $r < 21$, [0,10.3]% for $r > 21$ and [0,11.1]% for LRG samples. Both M05 and this work directly use the catalog from PHOTO pipeline, and the selection bias from M05 and our catalog will not differ from each other significantly. Following Eq.19 in M05, the selection bias is calculated,

$$\frac{\delta\gamma}{\gamma} = \frac{R_{min}(1 - R_{min})}{R} e_{rms}^2 n(R_{min}) \quad (\text{B1})$$

where R is the shear responsivity and $n(R_{min}) = 1.6, 2.4$ and 2.8 for $r < 21$, $r > 21$ and LRG samples in M05. We take the extreme value here that the $n(R_{min})$ for our sample is 2.4 .

PSF reconstruction bias

This bias arises from the process of reconstructing the PSF from the PHOTO PSF pipeline. This bias estimated in M05 is ± 2.1 to ± 2.5 for SDSS sample. The PSF applied in M05 and this work are both from PHOTO PSF pipeline. Following M05, we also use Eq. 20 in Hirata et al. (2004) to estimate this bias,

$$\frac{\delta\gamma}{\gamma} = (\mathcal{R}^{-1} - 1) \frac{\delta T^p}{T^p}. \quad (\text{B2})$$

Here, we fix $\frac{\delta T^p}{T^p}$ to be 0.03 as in H04 due to the same PSF reconstruction pipeline and the size of the PSF T varies very little. The estimated bias is ± 2.2 per cent which is consistent with M05 at ± 2.1 per cent for $r < 21$ and ± 2.4 per cent for $r > 21$. Ours is between the two values because we use all the galaxies with r band model magnitude to calculate the bias.

PSF dilution bias

The PSF blurs the image due to the convolution, which is a function of resolution \mathcal{R} and brightness distribution. An empirical formula of this bias from an ensemble of exponential and de Vaucouleurs distributions is given in M05 as a function of the fraction of exponential part and the fraction of de Vaucouleurs part,

$$\frac{\delta\gamma}{\gamma} \geq -0.014f_{exp} - 0.035f_{deV}. \quad (\text{B3})$$

Roughly, this value ranges from -2.8 to 3.9 percent. As both works use PHOTO PSF pipeline and because this bias is estimated in a model dependent method, here we directly use M05's estimation as shown in Table. 6 (* in Table. 6 indicates that we directly use M05's result here).

Shear responsivity error

The responsivity R is calculated from the variance of ellipticity, indicating that this is related to the ellipticity distribution. Once we use the cut $\mathcal{R} > 1/3$, the distribution has been changed and leading to the error on R . It ranges from 0 to 1.7% in M05. Our estimated bias using Eq. 25 in H04 is 2.3% with a fixed δe_{rms} to be 0.02 as in H04.

Noise rectification bias

This noise, ranging from -3.8 to 0% , is caused by the noise in images as described in HS03 (Eq.26 and Eq.27). The quantification of this bias is,

$$\frac{\delta\gamma}{\gamma} \approx Kv^{-2} = 4(1 - 3R_2^{-1} + R_2^{-2} + 2e_{rms}^2)v^{-2}, \quad (\text{B4})$$

where v is the signal-to-noise ratio of the detection over bands $v^{-2} = \frac{2}{v_r^2 + v_i^2}$. Our K at $\mathcal{R} = 1/3$ is 5.7 bigger than 5.3 in M05 and 5.1 in H04. So the lower limit of this bias (2σ) in our sample is -4.08 per cent larger than M05 and H04.

Systematic tests

In order to observationally estimate the systematics, three additional tests are carried out: redshift test, random sample test and 45 degree rotation test. Any systematics will lead these tests deviating from zero.

Redshift test

First, the redshift test. The lens-source separation for shear calculation is $z_l < z_s + 0.1$ to avoid the case that the source galaxy locate in front of the lens galaxy considering the typical photometric redshift measurement error is 0.025 (Abazajian et al. 2009). No signal is expected if we use the criterion $z_l > z_s$, and any non-zero value is from unknown systematics. Fig. 11 shows this systematic test using our SDSS DR7 data. The consistency with zero illustrates the fact that the systematic in our work can be neglected comparing to the null lensing signals shown in Fig. 11.

Random sample test

The random sample we use to test the systematic is from (Yang et al. 2012), which is also used to calculate the two point correlation function. This random sample includes all the observational effect from SDSS DR7, i.e., the same luminosity function, magnitude limit cut, the redshift completeness, the sky coverage due to the SDSS mask (MANGLE by Hamilton & Tegmark (2004)). The total number of random galaxy sample is 736812 , slightly more than the real sample we used to measure the lensing signals. We bin the random sample within the same 6 luminosity ranges and measure the galaxy-galaxy lensing signals around the random samples. Fig.12 shows the signals obtained around the random samples, which is consistent with null signals within one sigma error as well.

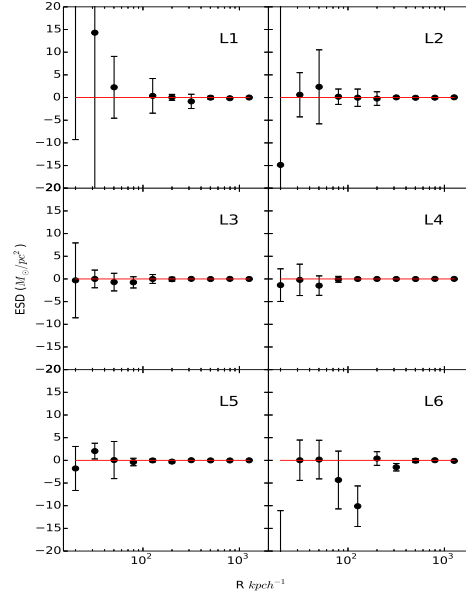


FIG. 11.— The redshift systematic check. Shown in the plot are the ESDs estimated using sources galaxies that are in front of the lens galaxies.

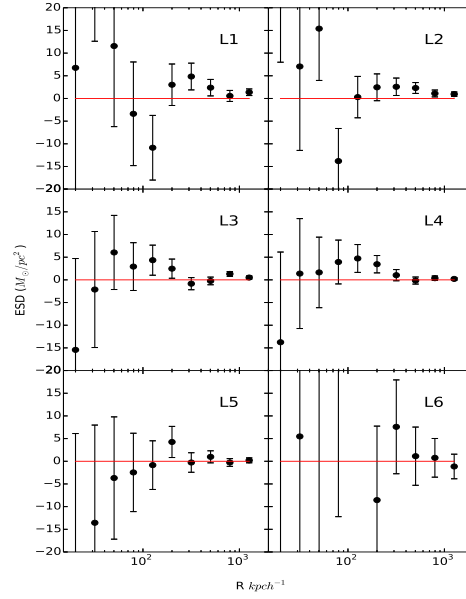


FIG. 12.— The random sample check. Shown in the plot are the ESDs estimated around random lens galaxies.

TABLE 7
THIS TABLE SHOWS THE RESULTS OF 45 DEGREE ROTATION TESTS AS IN M05.

Radial range($h^{-1}\text{kpc}$)	$\Delta\Sigma_{45}(hM_{\odot}\text{pc}^{-2})$	σ_{45}
$30 < R < 100$	-0.46	1.42
$100 < R < 600$	0.02	0.24
$600 < R < 2000$	-0.01	0.10
$30 < R < 2000$	-0.11	0.12

45 degree rotation test

Finally, we calculate the B mode signal using all the galaxies as did in M05, which calculate the 45 rotated signals with 4 distance bins, i.e., $30 < R < 100 h^{-1} \text{kpc}$, $100 < R < 600 h^{-1} \text{kpc}$, $600 < R < 2000 h^{-1} \text{kpc}$ and $30 < R < 2000 h^{-1} \text{kpc}$. Again, this systematic is consistent with zero within one sigma error.

C. THE ESDS OF LENS GALAXIES

Here we provide the related ESDs measured for our SDSS DR7 lens galaxies that are separated in different luminosity and stellar mass bins in the following two tables. Additional ESDs for galaxies that are separated into color and star formation subsamples, together with *all* the related covariance matrixes are provided in electronic files which are available via the link (http://gax.shao.ac.cn/wtluo/weak_lensing/wl_sdss_dr7.tar).

TABLE 8
THIS TABLE LISTS THE ESDS OF LENS GALAXIES THAT ARE SEPARATED INTO DIFFERENT LUMINOSITY BINS

$RMpc/h$	L1	L2	L3	L4	L5	L6
0.020	47.753 ± 51.318	22.722 ± 31.109	59.068 ± 21.041	85.001 ± 17.596	270.283 ± 19.675	395.426 ± 112.376
0.032	50.609 ± 29.971	29.589 ± 19.232	28.174 ± 13.808	59.956 ± 12.268	58.845 ± 15.307	199.987 ± 50.518
0.050	27.104 ± 18.650	6.401 ± 12.476	35.059 ± 8.693	33.181 ± 7.948	54.852 ± 12.084	96.381 ± 45.461
0.080	0.760 ± 11.775	8.969 ± 7.692	18.018 ± 5.313	27.231 ± 5.129	35.538 ± 8.089	111.051 ± 31.248
0.126	6.225 ± 7.465	8.183 ± 5.040	9.380 ± 3.491	12.053 ± 3.055	21.476 ± 4.981	105.765 ± 22.670
0.200	7.674 ± 4.772	6.517 ± 3.260	12.707 ± 2.162	11.417 ± 1.920	17.160 ± 3.042	54.225 ± 13.056
0.317	3.839 ± 3.063	3.512 ± 1.990	4.422 ± 1.381	8.229 ± 1.269	14.231 ± 1.957	38.240 ± 8.547
0.502	1.463 ± 1.929	5.645 ± 1.282	4.528 ± 0.860	4.891 ± 0.783	11.296 ± 1.183	18.851 ± 4.931
0.796	2.557 ± 1.266	4.166 ± 0.797	4.106 ± 0.551	3.616 ± 0.526	5.322 ± 0.758	17.179 ± 3.135
1.261	4.227 ± 0.773	3.990 ± 0.561	3.191 ± 0.358	2.979 ± 0.333	4.735 ± 0.499	10.577 ± 1.931

TABLE 9
THIS TABLE LISTS THE ESDS OF LENS GALAXIES THAT ARE SEPARATED INTO DIFFERENT STELLAR MASS BINS

$RMpc/h$	sm1	sm2	sm3	sm4	sm5	sm6	sm7
0.020	-4.333 ± 37.732	32.952 ± 31.256	82.383 ± 21.056	182.637 ± 21.271	335.980 ± 33.494	336.404 ± 30.651	115.285 ± 99.517
0.032	36.117 ± 25.027	-14.994 ± 19.186	41.799 ± 14.208	91.604 ± 15.367	43.176 ± 21.400	31.518 ± 22.789	256.227 ± 58.129
0.050	16.766 ± 15.203	30.626 ± 12.198	34.166 ± 9.904	44.174 ± 11.545	73.646 ± 18.962	66.753 ± 18.781	123.575 ± 45.973
0.080	21.305 ± 9.069	10.033 ± 7.549	20.878 ± 5.701	33.090 ± 7.798	52.717 ± 12.550	49.856 ± 13.153	113.419 ± 35.431
0.126	10.617 ± 5.837	13.010 ± 4.850	5.807 ± 3.915	23.703 ± 4.843	38.787 ± 8.170	40.202 ± 7.755	114.243 ± 25.088
0.200	7.286 ± 3.841	12.030 ± 3.186	14.715 ± 2.401	12.398 ± 2.847	24.732 ± 4.965	23.755 ± 4.770	65.843 ± 15.455
0.317	3.062 ± 2.413	3.039 ± 1.921	9.233 ± 1.482	9.110 ± 1.803	22.772 ± 3.356	22.250 ± 3.147	43.172 ± 9.255
0.502	3.836 ± 1.496	3.722 ± 1.273	5.069 ± 0.965	9.217 ± 1.174	15.316 ± 2.050	14.874 ± 1.904	22.356 ± 5.645
0.796	2.573 ± 0.975	3.312 ± 0.817	3.807 ± 0.605	4.872 ± 0.726	7.290 ± 1.218	7.172 ± 1.273	21.094 ± 3.776
1.262	2.929 ± 0.570	3.503 ± 0.497	3.155 ± 0.383	4.023 ± 0.480	5.760 ± 0.786	5.703 ± 0.749	12.316 ± 2.337

REFERENCES

- Abazajian, K. N., Adelman-McCarthy, J. K., Agüeros, M. A., et al. 2009, *ApJS*, 182, 543
 Alam, S., Albareti, F. D., Allende Prieto, C., et al. 2015, *arXiv:1501.00963*
 Amara, A., Metcalf, R. B., Cox, T. J., & Ostriker, J. P. 2006, *MNRAS*, 367, 1367
 Amara, A., & Réfrégier, A. 2007, *MNRAS*, 381, 1018
 Bacon, D. J., & Taylor, A. N. 2003, *MNRAS*, 344, 1307
 Bell, E. F., McIntosh, D. H., Katz, N., & Weinberg, M. D. 2003, *ApJS*, 149, 289
 Bartelmann, M., & Schneider, P. 2001, *Phys. Rep.*, 340, 291
 Bernstein, G. M., & Jarvis, M. 2002, *AJ*, 123, 583
 Bernstein, G. M. 2009, *ApJ*, 695, 652
 Bernstein, G. M., & Armstrong, R. 2014, *MNRAS*, 438, 1880
 Bertin, E., & Arnouts, S. 1996, *A&AS*, 117, 393
 Blanton, M. R., Brinkmann, J., Csabai, I., et al. 2003, *AJ*, 125, 2348
 Blanton, M. R., Schlegel, D. J., Strauss, M. A., et al. 2005, *AJ*, 129, 2562
 Bridle, S. L., Kneib, J.-P., Bardeau, S., & Gull, S. F. 2002, *The Shapes of Galaxies and their Dark Halos*, 38
 Bridle, S., Shawe-Taylor, J., Amara, A., et al. 2009, *Annals of Applied Statistics*, 3, 6
 Broadhurst, T., Benítez, N., Coe, D., et al. 2005, *ApJ*, 621, 53
 Cabanac, R. A., Fort, B., Gavazzi, R., & SL2S Team 2006, *SF2A-2006: Semaine de l'Astrophysique Française*, 329
 Cabanac, R. A., Alard, C., Dantel-Fort, M., et al. 2007, *A&A*, 461, 813
 Cacciato, M., van den Bosch, F. C., More, S., et al. 2009, *MNRAS*, 394, 929
 Chae, K.-H. 2003, *MNRAS*, 346, 746
 Covone, G., Kneib, J.-P., Soucail, G., et al. 2006, *A&A*, 456, 409
 Cropper, M., Hoekstra, H., Kitching, T., et al. 2013, *MNRAS*, 431, 3103
 Csabai, I., Budavári, T., Connolly, A. J., et al. 2003, *AJ*, 125, 580
 Dalal, N., Hennawi, J. F., Holder, G., & Bode, P. 2005, *Gravitational Lensing Impact on Cosmology*, 225, 193
 Fischer, P., McKay, T. A., Sheldon, E., et al. 2000, *AJ*, 120, 1198
 Fu, L., Semboloni, E., Hoekstra, H., et al. 2008, *A&A*, 479, 9
 George, M. R., Leauthaud, A., Bundy, K., et al. 2012, *ApJ*, 757, 2
 Griffiths, R. E., Casertano, S., Im, M., & Ratnatunga, K. U. 1996, *MNRAS*, 282, 1159
 Gunn, J. E., Carr, M., Rockosi, C., et al. 1998, *AJ*, 116, 3040
 Hamilton, A. J. S., & Tegmark, M. 2004, *MNRAS*, 349, 115
 Heymans, C., Brown, M., Heavens, A., et al. 2004, *MNRAS*, 347, 895
 Heymans, C., Brown, M. L., Barden, M., et al. 2005, *MNRAS*, 361, 160

- Heymans, C., Van Waerbeke, L., Bacon, D., et al. 2006, *MNRAS*, 368, 1323
- Heymans, C., Van Waerbeke, L., Miller, L., et al. 2012, *MNRAS*, 427, 146
- Hirata, C., & Seljak, U. 2003, *MNRAS*, 343, 459
- Hirata, C. M., Mandelbaum, R., Seljak, U., et al. 2004, *MNRAS*, 353, 529
- Hirata, C. M., Ho, S., Padmanabhan, N., Seljak, U., & Bahcall, N. A. 2008, *Phys. Rev. D*, 78, 043520
- Hoekstra, H., Franx, M., & Kuijken, K. 2000, *ApJ*, 532, 88
- Hoekstra, H., Franx, M., Kuijken, K., & Squires, G. 1998, *ApJ*, 504, 636
- Hoekstra, H., & Jain, B. 2008, *Annual Review of Nuclear and Particle Science*, 58, 99
- Kaifu, N. 1998, *Proc. SPIE*, 3352, 14
- Kaiser, N., Squires, G., & Broadhurst, T. 1995, *ApJ*, 449, 460
- Kaiser, N. 2000, *ApJ*, 537, 555
- Kauffmann, G., Heckman, T. M., White, S. D. M., et al. 2003, *MNRAS*, 341, 33
- Kitching, T. D., Miller, L., Heymans, C. E., van Waerbeke, L., & Heavens, A. F. 2008, *MNRAS*, 390, 149
- Kitching, T., Balan, S., Bernstein, G., et al. 2010, *arXiv:1009.0779*
- Kilbinger, M., Fu, L., Heymans, C., et al. 2013, *MNRAS*, 430, 2200
- Kneib, J.-P., Ellis, R. S., Santos, M. R., & Richard, J. 2004, *ApJ*, 607, 697
- Kneib, J.-P. 2006, *HST Proposal*, 10876
- Koekemoer, A. M., Aussel, H., Calzetti, D., et al. 2007, *ApJS*, 172, 196
- Kuijken, K., Heymans, C., Hildebrandt, H., et al. 2015, *MNRAS*, 454, 3500
- Leauthaud, A., Massey, R., Kneib, J.-P., et al. 2007, *ApJS*, 172, 219
- Leauthaud, A., Tinker, J., Bundy, K., et al. 2012, *ApJ*, 744, 159
- Li, R., Mo, H. J., Fan, Z., et al. 2009, *MNRAS*, 394, 1016
- Li, R., Mo, H. J., Fan, Z., Yang, X., & Bosch, F. C. v. d. 2013, *MNRAS*, 430, 3359
- Li, R., Shan, H., Mo, H., et al. 2014, *MNRAS*, 438, 2864
- Liu, X., Pan, C., Li, R., et al. 2014, *arXiv:1412.3683*
- LSST Science Collaboration, Abell, P. A., Allison, J., et al. 2009, *arXiv:0912.0201*
- Luo, W., Yang, X., & Zhang, Y. 2014, *ApJ*, 789, L16
- Lupton, R., Gunn, J. E., Ivezić, Z., Knapp, G. R., & Kent, S. 2001, *Astronomical Data Analysis Software and Systems X*, 238, 269
- Jarvis, M., Sheldon, E., Zuntz, J., et al. 2015, *arXiv:1507.05603*
- Mandelbaum, R., Hirata, C. M., Seljak, U., et al. 2005, *MNRAS*, 361, 1287
- Mandelbaum, R., Seljak, U., Kauffmann, G., Hirata, C. M., & Brinkmann, J. 2006, *MNRAS*, 368, 715
- Mandelbaum, R., Seljak, U., Hirata, C. M., et al. 2008, *MNRAS*, 386, 781
- Mandelbaum, R., van de Ven, G., & Keeton, C. R. 2009a, *MNRAS*, 398, 635
- Mandelbaum, R., Li, C., Kauffmann, G., & White, S. D. M. 2009b, *MNRAS*, 393, 377
- Mandelbaum, R., Hirata, C. M., Leauthaud, A., Massey, R. J., & Rhodes, J. 2012, *MNRAS*, 420, 1518
- Mandelbaum, R., Slosar, A., Baldauf, T., et al. 2013, *MNRAS*, 432, 1544
- Mandelbaum, R., Rowe, B., Bosch, J., et al. 2014, *ApJS*, 212, 5
- Mandelbaum, R., Rowe, B., Armstrong, R., et al. 2015, *MNRAS*, 450, 2963
- Maoli, R., Mellier, Y., van Waerbeke, L., et al. 2000, *The Messenger*, 101, 10
- Massey, R., & Refregier, A. 2005, *MNRAS*, 363, 197
- Massey, R., Rhodes, J., Leauthaud, A., et al. 2007a, *ApJS*, 172, 239
- Massey, R., Heymans, C., Bergé, J., et al. 2007b, *MNRAS*, 376, 13
- Massey, R., Stoughton, C., Leauthaud, A., et al. 2010, *MNRAS*, 401, 371
- Massey, R., Hoekstra, H., Kitching, T., et al. 2013, *MNRAS*, 429, 661
- Miller, L., Kitching, T. D., Heymans, C., Heavens, A. F., & van Waerbeke, L. 2007, *MNRAS*, 382, 315
- Miller, L., Heymans, C., Kitching, T. D., et al. 2013, *MNRAS*, 429, 2858
- Mo, H., van den Bosch, F. C., & White, S. 2010, *Galaxy Formation and Evolution*. Cambridge University Press, 2010. ISBN: 9780521857932
- Motohara, K., Takata, T., Iwamuro, F., et al. 2005, *AJ*, 129, 53
- Nakajima, R., & Bernstein, G. 2007, *AJ*, 133, 1763
- Navarro, J. F., Frenk, C. S., & White, S. D. M. 1997, *ApJ*, 490, 493
- Oguri, M., Taruya, A., Suto, Y., & Turner, E. L. 2002, *ApJ*, 568, 488
- Oguri, M., Hennawi, J. F., Gladders, M. D., et al. 2009, *ApJ*, 699, 1038
- Oguri, M., Takada, M., Okabe, N., & Smith, G. P. 2010, *MNRAS*, 405, 2215
- Okabe, N., Futamase, T., Kajisawa, M., & Kuroshima, R. 2014, *ApJ*, 784, 90
- Refregier, A. 2003, *ARA&A*, 41, 645
- Refregier, A., Amara, A., Kitching, T. D., et al. 2010, *arXiv:1001.0061*
- Rhodes, J., Refregier, A., & Groth, E. J. 2000, *ApJ*, 536, 79
- Rhodes, J. D., Massey, R. J., Albert, J., et al. 2007, *ApJS*, 172, 203
- Rowe, B. T. P., Jarvis, M., Mandelbaum, R., et al. 2015, *Astronomy and Computing*, 10, 121
- Scoville, N., Abraham, R. G., Aussel, H., et al. 2007a, *ApJS*, 172, 38
- Scoville, N., Aussel, H., Brusa, M., et al. 2007b, *ApJS*, 172, 1
- Sheldon, E. S., Johnston, D. E., Frieman, J. A., et al. 2004, *AJ*, 127, 2544
- Sheldon, E. S., Johnston, D. E., Scranton, R., et al. 2009, *ApJ*, 703, 2217
- Simet, M., Kubo, J. M., Dodelson, S., et al. 2012, *ApJ*, 748, 128
- Strauss, M. A., Weinberg, D. H., Lupton, R. H., et al. 2002, *AJ*, 124, 1810
- Tortora, C. 2007, *1st Workshop of Astronomy and Astrophysics for Students*, 127
- Treu, T., Koopmans, L. V., Bolton, A. S., Burles, S., & Moustakas, L. A. 2006, *ApJ*, 640, 662
- Umetsu, K., Tanaka, M., Kodama, T., et al. 2005, *PASJ*, 57, 877
- Umetsu, K. 2007, *Subaru Proposal*, 24
- Umetsu, K., Medezinski, E., Nonino, M., et al. 2014, *ApJ*, 795, 163
- van den Bosch, F. C., Norberg, P., Mo, H. J., & Yang, X. 2004, *MNRAS*, 352, 1302
- van Waerbeke, L. 2001, *Cosmological Physics with Gravitational Lensing*, 165
- Walsh, D., Wills, B. J., & Wills, D. 1979, *MNRAS*, 189, 667
- Wang, L., Yang, X., Shen, S., et al. 2014, *MNRAS*, 439, 611
- Wittman, D., Dell'Antonio, I. P., Hughes, J. P., et al. 2006, *ApJ*, 643, 128
- Yang, X. H., Mo, H. J., Kauffmann, G., & Chu, Y. Q. 2003, *MNRAS*, 339, 387
- Yang, X., Mo, H. J., van den Bosch, F. C., et al. 2006a, *MNRAS*, 373, 1159
- Yang, X., Mo, H. J., & van den Bosch, F. C. 2006b, *ApJ*, 638, L55
- Yang, X., Mo, H. J., van den Bosch, F. C., et al. 2007, *ApJ*, 671, 153
- Yang, X., Mo, H. J., & van den Bosch, F. C. 2008, *ApJ*, 676, 248
- Yang, X., Mo, H. J., van den Bosch, F. C., Zhang, Y., & Han, J. 2012, *ApJ*, 752, 41
- Yang, X., Mo, H. J., van den Bosch, F. C., et al. 2013, *ApJ*, 770, 115
- York, D. G., Adelman, J., Anderson, J. E., Jr., et al. 2000, *AJ*, 120, 1579
- Zhang, J. 2010, *MNRAS*, 403, 673
- Zhang, J. 2011, *JCAP*, 11, 041
- Zhang, J., Luo, W., & Foucaud, S. 2015, *JCAP*, 1, 024
- Zu, Y., Weinberg, D. H., Jennings, E., Li, B., & Wyman, M. 2014, *MNRAS*, 445, 1885
- Zu, Y., & Weinberg, D. H. 2013, *MNRAS*, 431, 3319